Geochimica et Cosmochimica Acta 373 (2024) 197–210

Contents lists available at ScienceDirect

Geochimica et Cosmochimica Acta

journal homepage: www.elsevier.com/locate/gca

New olivine morphologies in shergottites reveal complex thermal histories of martian magmas

S.A. Eckley[a,b,*], R.A. Ketcham[b], Y. Liu[c], A. Udry[d], J. Gross[e,f,g,h]

[a] Jacobs – JETS, Astromaterials Research and Exploration Science Division, NASA Johnson Space Center, Houston, TX, USA
[b] Jackson School of Geosciences, The University of Texas at Austin, Austin, TX, USA
[c] Jet Propulsion Laboratory, California Institute of Technology, Pasadena, CA, USA
[d] Department of Geoscience, University of Nevada Las Vegas, Las Vegas, NV, USA
[e] Department of Earth and Planetary Sciences, Rutgers University, Piscataway, NJ, USA
[f] Department of Earth and Planetary Sciences, American Museum of Natural History, New York, NY, USA
[g] Lunar and Planetary Institute, Houston, TX, USA
[h] NASA Johnson Space Center, Houston, TX, USA

ARTICLE INFO

Associate editor: Tomohiro Usui

Keywords:
Shergottites
Martian meteorites
Olivine
Thermal history
X-ray computed tomography
Skeletal
Dendritic
Rapid growth
Mars

ABSTRACT

Petrogenetic models of martian magmas reflect the compositional, thermal, and geodynamical evolution of its interior. Most models for shergottite meteorites, which sampled relatively young martian basalts, invoke partial melting in a mantle plume head and filtering of the magma through the crust. Olivine-phyric, poikilitic, and olivine-gabbroic shergottites contain large, Mg-rich olivine crystals that record their parent magma history and are generally regarded to form initially in slow cooling, near-equilibrium environments in the lower crust. Here we report the unexpected common occurrence of Mg-rich olivine crystals with chained, mantled dendritic, and skeletal morphologies that reflect rapid growth, requiring relatively large degrees of undercooling and possibly moderate to fast cooling rates. Novel 3D analysis of crystal textures and core Fe-Mg content demonstrates that chained and mantled dendritic olivines in enriched shergottites are among the earliest-formed crystals, indicating rapid crystal growth during initial magma pooling in the lower crust, a process that has not been documented in Earth basalts. In geochemically depleted shergottites, skeletal olivines appear later in the crystallization sequence, but before the final eruption and solidification. Geochemically intermediate samples do not contain rapid-growth olivine, indicating extended equilibrium growth. The frequent occurrence of chained, mantled dendritic, and skeletal olivines in enriched and depleted shergottites suggests that the conditions needed for rapid growth are common for mafic magmatism on Mars, and that these magmas experience complex thermal histories characterized by discrete episodes of large undercooling at depth.

1. Introduction

Igneous processes on Mars provide a window into the planet's internal structure and thermal profile. Such processes can be studied through textural and mineralogical analysis of martian shergottites—largely mafic to ultramafic rocks with a variety of igneous textures (e.g., Udry et al., 2020). The olivine-phyric, poikilitic, and olivine gabbroic shergottite subclasses contain large (up to ~ 3 mm) olivine crystals that grew over a wide range of thermodynamic conditions. Their texture and composition record the physico-chemical evolution of their parent magma from initial crystallization to final emplacement, making them especially useful for tracking magmatic processes throughout the martian crust.

The large, Mg-rich olivine crystals within olivine-phyric, poikilitic, and olivine gabbroic shergottites are the first silicate phases to crystallize from their parent magmas, which is thought to occur in staging magma chambers within the martian crust (e.g., Filiberto et al., 2010; Gross et al., 2013; Howarth et al., 2014; Liu et al., 2016). Thermobarometric work using the Al/Ti-in-pyroxene model and/or thermodynamic phase diagram calculations of multiply-saturated phases indicates that olivine crystallization within all three of these shergottite subclasses initiated at 40 km to 85 km deep and ~ 1390 °C to 1500 °C, corresponding to depths in the middle to lower crust, and possibly at/near the crust-mantle boundary (Musselwhite et al., 2006; Usui et al., 2008;

---

[*] Corresponding author at: Jacobs – JETS, Astromaterials Research and Exploration Science Division, NASA Johnson Space Center, Houston, TX, USA.
E-mail address: scott.a.eckley@nasa.gov (S.A. Eckley).

https://doi.org/10.1016/j.gca.2024.04.006
Received 4 July 2023; Accepted 4 April 2024
Available online 6 April 2024

Filiberto et al., 2010; Usui et al., 2012; Balta et al., 2013; Gross et al., 2013; Howarth et al., 2014; Balta et al., 2015; Basu Sarbadhikari et al., 2016; Liu et al., 2016; Dunham et al., 2019; Rahib et al., 2019; Udry et al., 2020). After this initial growth phase at depth, the olivine-phyric, poikilitic, and olivine gabbroic shergottites experienced varied petrogenetic histories, described below.

Olivine-phyric shergottites have a porphyritic texture of large (from ~ 0.5 mm to 3 mm) Mg-rich olivine crystals, commonly referred to as megacrysts, set in a finer-grained groundmass of mostly pyroxene and plagioclase (shocked to maskelynite) (e.g., Barrat et al., 2002; Goodrich, 2002; Usui et al., 2008; Basu Sarbadhikari et al., 2009; Filiberto et al., 2010; Gross et al., 2013; Liu et al., 2013; Ennis and McSween, 2014; Balta et al., 2015; Liu et al., 2016; Dunham et al., 2019). Megacryst olivine began to crystallize within magma chambers in the middle to lower crust, but the duration of olivine growth at depth varied and the relationship of olivine crystals to the final host magma is debated (Barrat et al., 2002; Goodrich, 2002; Basu Sarbadhikari et al., 2009; Liu et al., 2013; Ennis and McSween, 2014; Balta et al., 2015; Basu Sarbadhikari et al., 2016; Liu et al., 2016; Dunham et al., 2019). These authors have variably interpreted megacryst olivine as xenocrysts (i.e., foreign crystals that are petrogenetically unrelated to their final host magma), phenocrysts (i.e., crystals that grew directly from their final host magma), or antecrysts (i.e., crystals that grew from the same magma system, but from an earlier, less evolved magma) based on textural and geochemical analyses. They have also noted that megacryst olivine generally display normal magmatic zoning of decreasing Mg content from core-to-rim, and occasionally high Fe content in thin rims. The shape and amplitude of core-to-rim Mg zoning patterns vary from sample-to-sample, which are interpreted to reflect Mg/Fe diffusion during differing residence times at elevated temperatures. Regardless of their origin, these crystal-laden magmas ascended through the crust, where olivine nucleation and growth likely continued from a more evolved melt, and were then either injected into the shallow subsurface or erupted onto the surface where the finer-grained groundmass crystallized and Fe-rich olivine rims formed around some samples during a final rapid cooling period. Poikilitic shergottites have large (cm-sized) irregularly shaped pyroxene crystals, referred to as oikocrysts, that enclose olivine chadacrysts (up to ~ 3 mm). These pyroxene-olivine assemblages formed in magma chambers in the middle to lower crust and were then entrained in an ascending magma. They were emplaced in the subsurface where a coarse-grained groundmass of mostly olivine, pyroxene, and plagioclase (shocked to maskelynite) crystallized (e.g., Usui et al., 2010; Howarth et al., 2014; Rahib et al., 2019). Olivine-gabbroic shergottites are a relatively new classification characterized by large, early-formed pyroxene (up to ~ 5 mm) and olivine (up to ~ 2 mm) that co-crystallized in magma chambers in the middle to lower crust and were then entrained in an ascending magma and emplaced near the surface where a medium- to fine-grained groundmass of mostly plagioclase (shocked to maskelynite) crystallized (Benaroya et al., 2024).

The early-formed olivines in olivine-phyric, poikilitic, and olivine-gabbroic shergottites have large sizes, euhedral to subhedral shapes, and chemical zoning that are generally interpreted to reflect long residence times of hundreds of days (Peslier et al., 2010; Ennis and McSween, 2014; Liu et al., 2016; Rahib et al., 2019), slow cooling rates of ~ 0.2 – 2.0 °C/h (Basu Sarbadhikari et al., 2009; Ennis and McSween, 2014; Balta et al., 2015), and near-equilibrium conditions (Basu Sarbadhikari et al., 2009; Peslier et al., 2010; Usui et al., 2010; Gross et al., 2011; Gross et al., 2013; Dunham et al., 2019; Mari et al., 2020) during growth at depth. However, previous work in many terrestrial environments has shown that large, well-formed olivine with a polyhedral external morphology, like those described in the shergottites above, can grow rapidly, as evidenced by internal skeletal textures and/or dendritic chemical zonation patterns, specifically P, Cr, and Al (Mattioli et al., 2006; Welsch et al., 2013; Welsch et al., 2014; Shea et al., 2015; Xing et al., 2017; Mourey and Shea, 2019; Albert et al., 2020; Salas et al., 2021).

Evidence for rapid growth can also be preserved through various external crystal morphologies. In early experimental work detailing olivine growth, Donaldson (1976) identified ten olivine morphologies and showed that there is a systematic correlation between crystal morphology and degree of undercooling and cooling rate. It was later shown by Faure et al. (2003) that there are only four primary morphologies depending on how the crystal is oriented – polyhedral, tabular, skeletal, and dendritic. Polyhedral olivine has well-defined faces and may contain spherical or elongated inclusions. Tabular olivine has well-defined faces, but with preferential growth along the a- and c-axes. Skeletal olivine, which are often called hopper olivine, has an hourglass morphology elongated along the a-axis. The top and bottom of the hourglass shape (i.e., "hoppers") are hollow and remained in contact with the surrounding melt. Dendritic olivine forms a variety of shapes, but generally contains thin bars or rods growing along the a-c plane from a central nucleus towards the crystal corners, sometimes with repeating and parallel branches.

Olivine with tabular, hopper/skeletal, and dendritic external morphologies, or polyhedral olivine with internal dendritic chemical zonation patterns, reflects relatively rapid growth rates due to moderate to extreme overstepping of crystallization conditions (e.g., Donaldson, 1976; Sunagawa, 1981; Faure et al., 2003; Mourey and Shea, 2019; Shea et al., 2019), usually linked to relatively large degrees of undercooling ($\Delta T = T_{liquidus} - T_{system}$) that are generally associated with, but not exclusively caused by, moderate to fast cooling rates. Such conditions are expected in extrusive settings, but only recently have these textures been documented in shallow magma chambers or during rapid magma ascent on Earth (Mattioli et al., 2006; Welsch et al., 2013; Mourey and Shea, 2019; Albert et al., 2020; Salas et al., 2021).

Despite the growing evidence for rapid crystal growth of megacryst-sized olivine in terrestrial environments, such evidence in shergottites has been limited. Early-formed polyhedral olivines with internal dendritic chemical zonation patterns are present in Allan Hills (ALHA) 77,005 (Milman-Barris et al., 2008) and Dhofar (Dho) 019 (Ennis and McSween, 2014), and only three thin sections containing olivines with putative skeletal or hopper external morphologies have been documented: two sections of Larkman Nunatak (LAR) 06,319 (Basu Sarbadhikari et al., 2009 – Fig. 1; Peslier et al., 2010 – Sec. 4.2.1) and one section of Tissint (Balta et al., 2015 – Fig. 2f).

Here we report the results of a novel 3D survey of the olivine crystal populations in fourteen shergottites with large, early-formed olivine using X-ray computed tomography (CT). We document the widespread occurrence of previously unrecognized olivine morphologies that are indicative of rapid growth. Combined with a sample-wide analysis of approximate forsterite (Fo) content at the true crystal core and crystal size in seven samples, we identify crystallization sequences that allow us to infer distinct relative thermal histories of the shergottite parent melts that are correlated with geochemical signatures. Olivines with rapid-growth morphologies are likely to be a ubiquitous feature in shergottites, which sample relatively young basalts, and possibly in older igneous martian rocks, indicating that there have been planet-wide processes leading to rapid olivine growth occurring over much of Mars' history.

2. Materials and methods

2.1. Materials

Chips of fourteen shergottites with large, early-formed olivine from the ANSMET collection (Larkman Nunatak [LAR] 06319,75; LAR 12011,54A; LAR 12095,40A; LAR 12240,27; Elephant Moraine [EETA] 79001,536 lithology A; and Roberts Massif [RBT] 04261,0), Dupont meteorite collection at the Chicago Field Museum (Tissint), and private dealers (Northwest Africa [NWA] 1068; NWA 7397; NWA 7755; NWA 11043; NWA 12241; NWA 13227; and NWA 14017) were obtained for this study (Tables 1 and S1; supplementary text).

Eight samples (LAR 12095, LAR 12240, Tissint, EETA 79001, LAR 12011, LAR 06319, NWA 1068, and NWA 14017) are classified as olivine-phyric (Table 1). LAR 12095 and LAR 12240 as well as LAR 06319 and LAR 12011 are paired samples. Five samples (NWA 12241, RBT 04261, NWA 7397, NWA 11043, and NWA 7755) are classified as poikilitic. This shergottite subclass is commonly characterized by "poikilitic" and "non-poikilitic" domains, which refer to the early-formed pyroxene-olivine assemblages and the later formed groundmass phases, respectively. As such, we refer to olivine that is three-dimensionally enclosed by a pyroxene oikocryst as "poikilitic olivine" and olivine in the groundmass as "non-poikilitic olivine". NWA 13227, which is a newly classified sample, is an olivine-gabbroic shergottite (Benaroya et al., 2024).

Further classification of shergottites into geochemically enriched, intermediate, or depleted categories is based on measured radiogenic isotopic ratios and light rare earth element concentrations that mostly reflect their mantle sources (e.g., Symes et al., 2008; Shafer et al., 2010; Lapen et al., 2017). Other factors, such as the number of distinct mantle sources and potential input from a crustal component, add further complications to the cause of these different geochemical categories (e.g., Udry et al., 2020). The samples in this study represent all three geochemical categories: enriched, intermediate, and depleted (Table 1). There is no correlation between the lithological and geochemical classifications (e.g., not all olivine-phyric shergottites are geochemically depleted).

2.2. *X-ray computed tomography (CT) scanning*

X-ray CT scanning was performed at the Astromaterials X-ray Computed Tomography Lab at NASA Johnson Space Center using a Nikon XTH 320 and at the University of Texas High-Resolution X-ray Computed Tomography Facility (UTCT) using either a custom-built North Star Imaging scanner or Zeiss 620 Versa. All three instruments produce the same type of data, but at different resolutions. Scanning conditions are summarized in Table S1. Software corrections were used to reduce beam hardening and ring artifacts during reconstruction. The final reconstructed data are output as a contiguous series of 2D 16-bit grayscale images (slices), which together comprise a 3D grid of cubic voxels (3D pixel) (Table S1). Each voxel's grayscale value, which we refer to as CT #, reflects the effective X-ray attenuation of the material comprising that voxel, which is a function of a material's atomic number (Z) and density, as well as X-ray energy. Phases with a higher relative X-ray attenuation (i.e. high-Z and high density) are generally visualized with brighter gray values (i.e., higher CT #) (Ketcham and Carlson, 2001).

2.3. *CT data processing*

We use Dragonfly™ software (Object Research Systems) to visualize CT data along obliquely oriented slices, create 3D volume renderings, measure sample volumes, crystal interfacial angles, and crystal axes lengths, and determine a crystal's mean central CT #.

2.4. *Olivine crystallographic indexing*

X-ray CT produces a 3D image of crystal shapes, which we use to derive the orientations of crystallographic axes based on interfacial angles between faces (i.e., Steno's 1st principle). As almost all olivine crystals in these samples are euhedral and have intact, or partially intact, exteriors, we measure the angle between crystal faces in 3D and compare them to known interfacial angles to determine the orientation of the crystallographic axes. See the supplementary information for crystallographic indexing methods.

2.5. *Measuring olivine axis length and approximate Fo content*

We measured the a-, b-, and c-axis length of 22–29 olivines with different morphologies per sample in LAR 12011, LAR 06319, RBT 04261, NWA 7397, LAR 12095, LAR 12240, and Tissint (Table 1 and S2). Only complete olivine crystals were measured; any olivine truncated by the sample boundary was excluded. The largest complete olivine (determined by the analyst) in each sample was included. A marker was placed on each olivine after measurement so that the same crystal was not counted more than once. The other seven samples were excluded from this analysis because their thin, slab-like shapes meant there were few complete crystals.

Within each of the olivine $[(Fe,Mg)_2SiO_4]$ crystals from the seven analyzed samples mentioned above, we measured the mean CT # (i.e., grayscale value) at the true crystal core (Table S2) and converted those to approximate forsterite (Mg-endmember) content ($Fo = \text{molar } 100 \times MgO/[MgO + FeO]$). We describe the conversion method below and in Appendix A and Tables S3 and S4. This technique takes advantage of the strong contrast in X-ray attenuation between Mg and Fe, and the ability to confidently locate the geometric center of each grain in 3D, which allows us to estimate the approximate Fo content of the true crystal core. Conversely, traditional thin/thick sections are typically prepared by random cutting with no 3D context, meaning the cut surface may not expose a true central plane. As such, without 3D context from CT scanning, only apparent crystal core and core-to-rim profiles can be analyzed on thin/thick sections.

The CT # at the true crystal core (Table S2) was determined by taking the mean CT # of a circle ($\sim$5 voxels in radius) in the middle of the central a-c plane. Inclusions (melt inclusions and oxide/sulfide inclusions) and fractures on the measured slice and several slices above

Table 1

Sample classification, olivine morphologies present, and Fo_{CT} measurement performed.

Sample	Classification		Skeletal	Mantled Dendritic	Chained	Fo_{CT} Measured
	Lithology	Geochemistry				
LAR 12095	Olivine-phyric	Depleted	x			x
LAR 12240	Olivine-phyric	Depleted	x			x
Tissint	Olivine-phyric	Depleted	x			x
EETA 79001	Olivine-phyric	Intermediate				
LAR 12011	Olivine-phyric	Enriched		x	x	x
LAR 06319	Olivine-phyric	Enriched	x	x		x
NWA 1068	Olivine-phyric	Enriched		x	x	
NWA 14017	Olivine-phyric	Unknown				
NWA 13227	Olivine gabbroic	Enriched		x		
NWA 12241	Poikilitic	Intermediate				
RBT 04261	Poikilitic	Enriched		x		x
NWA 7397	Poikilitic	Enriched		x		x
NWA 11043	Poikilitic	Enriched		x		
NWA 7755	Poikilitic	Enriched		x		

and below were excluded so that only olivine was measured and local partial volume and blurring effects were avoided (Ketcham and Mote, 2019). The mean CT # was then converted to approximate Fo content, hereafter referred to as Fo_{CT}, using direct CT # – Fo calibration or calibration using literature Fo data.

We generated direct CT # – Fo calibration curves using EPMA analysis of olivines in sections cut with corresponding CT data (Fig. 1; Table S3). We used the CT data for LAR 12095 and LAR 12011 to prepare polished thick sections (LAR 12095,50 and LAR 12011, 61) that bisected the middle of the largest olivine crystal that did not touch the sample boundary (Fig. 1). Core Fo content was measured on 5 and 7 olivine crystals in LAR 12095 and LAR 12011, respectively, using a CAMECA SX-100 at NASA Johnson Space Center. Analytical details are found in the supplementary material. The CT slices that corresponded to the thick section surfaces were manually found using Dragonfly™ software and the CT # was measured at the corresponding EPMA analysis site using small (25 μm to 100 μm radius) circular regions-of-interest (ROI) (Fig. 1). We used these ground truth data to create calibration curves that show there is a linear relationship between CT # and Fo content within the CT datasets for LAR 12095 and LAR 12011 ($R^2 = 0.97$ and 0.98, respectively) (Fig. S1). The calibration curves were then used to convert the CT # that was measured in other olivines throughout the rest of LAR 12095 and LAR 12011 to FoCT content (Table S2).

The second approach is to generate CT # – Fo calibration curves using published olivine core and rim Fo values measured with EPMA (Table S4) (Basu Sarbadhikari et al., 2009; Usui et al., 2010; Howarth et al., 2014; Liu et al., 2016). We used the minimum and maximum literature Fo values for the pairing groups LAR 12095/LAR 12,240 and LAR 06319/LAR 12011. The highest EPMA-measured core Fo value corresponded to the lowest core CT #. Another ~ 5 voxel radius circle was used to calculate the mean CT # of rims of five olivine crystals from each sample. The highest mean rim CT # corresponded to the lowest EPMA-measured olivine rim Fo value. The EPMA-measured Fo values and the mean CT # values for the most Mg-rich core and least Mg-rich rim were used to create a linear conversion of CT # to approximate Fo_{CT} content at each crystal's true core for every sample (Table S4).

We tested the reproducibility of the two approaches on LAR 12095 and LAR 12011. FoCT data determined using the literature's Fo Min/Max conversion, referred to as "FoCT-literature", are almost identical to the FoCT determined using the ground truth data conversion, referred to as "FoCT-ground truth", in LAR 12011. The average difference between FoCT-ground truth and FoCT-literature is −1 (range from −2 to + 1) (Fig. S2). The average difference between FoCT-ground truth and FoCT-literature in LAR 12095 is −2, but the range is much larger, from −8 to

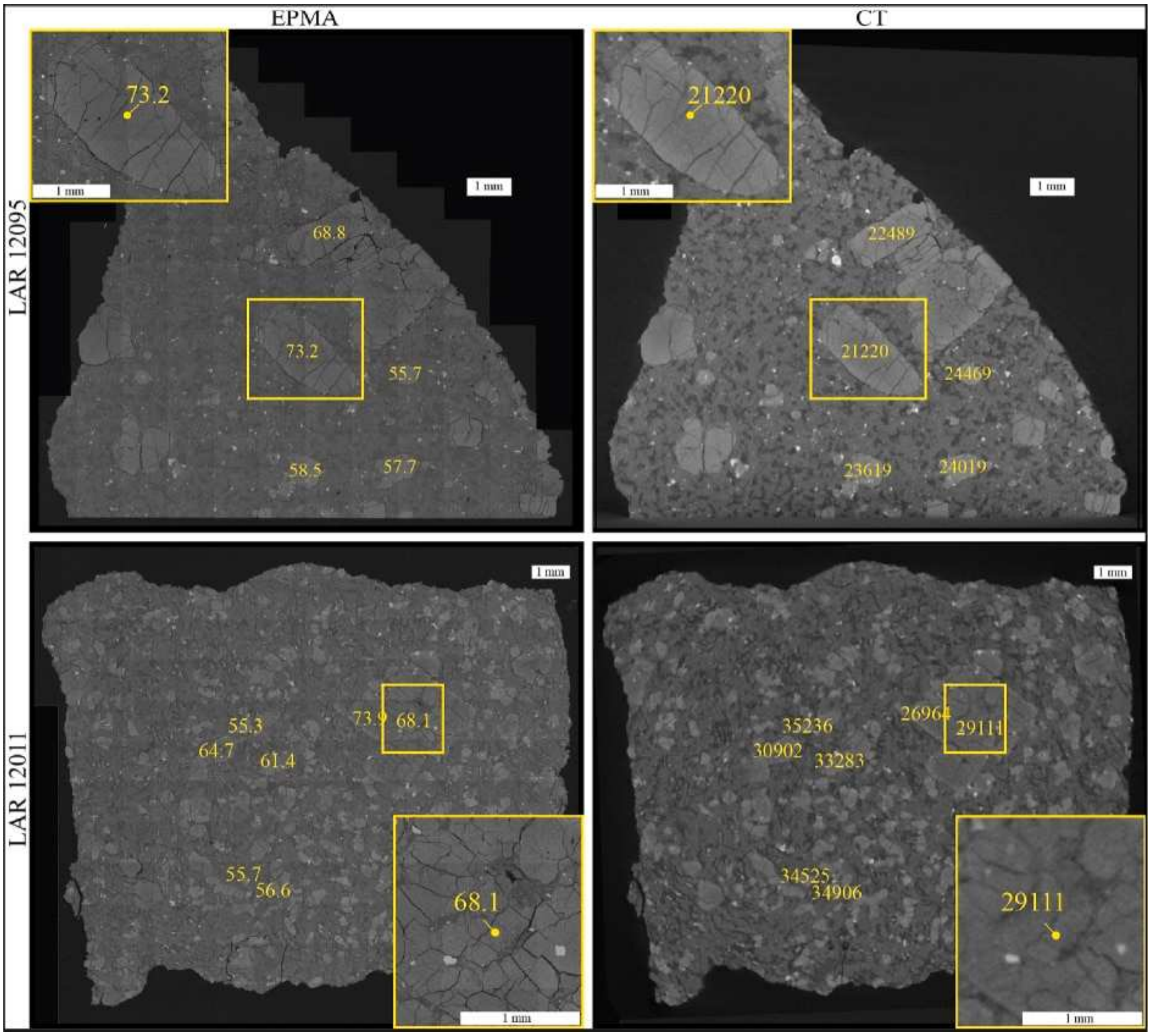

Fig. 1. Correlated EPMA and CT # in olivine. Backscatter electron (BSE) mosaic images (left) and the corresponding X-ray CT slice (right) for LAR 12095 (top) and LAR 12011 (bottom). Olivine Fo content and CT # (yellow text for both) were analyzed at the same spots on the thick section and corresponding CT slice, respectively.

+ 5 (Fig. S2). A likely cause for this discrepancy may be that LAR 12095 (and its pair LAR 12240) are relatively unstudied samples and that thin section analysis of core and rim Fo content may not provide a representative range compared to what can be measured when evaluating a larger sample volume with CT. A limited Min/Max literature range limits the FoCT range, but the overall trends in FoCT contents vs. crystal size (Fig. S3) and their interpretations do not change.

3. Results

3.1. New olivine morphologies in shergottites

Most samples in this study have been extensively examined by previous researchers, including detailed petrographic and petrologic analyses of traditionally prepared thin/thick sections (e.g., Barrat et al., 2002; Goodrich, 2003; Basu Sarbadhikari et al., 2009; Usui et al., 2010; Howarth et al., 2014; Balta et al., 2015; Liu et al., 2016; Dunham et al.,

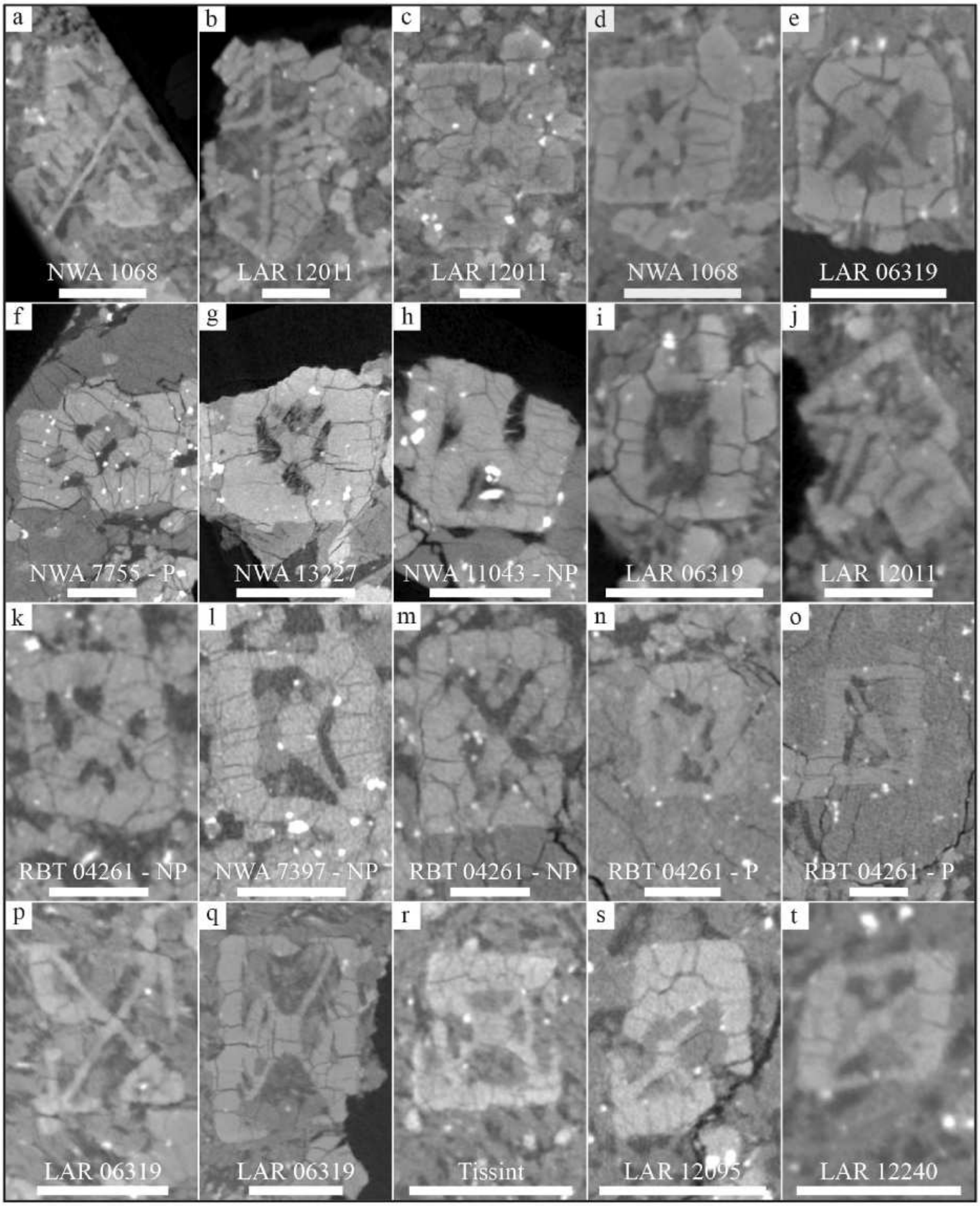

Fig. 2. Rapid-growth olivine. CT slices from central sections of olivines oriented orthogonally to the b-axis (i.e, [0 1 0]). A – B (chained); C – O (mantled dendritic); P – T (skeletal). NP = non-poikilitic domain; P = poikilitic domain. All scale bars are 1 mm.

2019; Rahib et al., 2019; Benaroya et al., 2024). The goal of this work is to describe new features in the olivine crystal population that are best, or only, seen in 3D.

We observed a subset of olivines with skeletal, mantled dendritic, or chained morphologies (described below) in eleven of the fourteen samples (Figs. 2 and 3; Table 1). Morphologies were ascertained by visualizing the 3D data along diagnostic planes, such as orthogonal to the b-axis (i.e., [0 1 0]; [0 1 0] is the zone orthogonal to the (0 1 0) crystal face). Olivines with these morphologies represent a small portion (usually less than ten for the samples $< 1000\ mm^3$) of the total olivine crystal population with the chained olivine representing the least common form among these three morphologies. Other morphologies, such as equant polyhedral that either have no melt inclusions or small, spherical ones, and tabular polyhedral with one or more large, elongated melt inclusions are more commonly found in all samples (Fig. 3).

Skeletal olivine have externally skeletal morphologies characterized by primary branches of olivine extending from the crystal center along the central [0 1 0] plane to the crystal corners {1 0 1} with repeating branches that are parallel to the crystal exterior and extending along the b-axis to form a 3D frame (Fig. 2P – 2T and 3). When viewed from all different directions, the sides of skeletal olivines in all samples are not fully closed and instead have reentrant features and hoppers that allowed the interior to remain in contact with the melt (Fig. 3). As such, the skeletal olivine in random 2D slices often retains skeletal forms or contain reentrant melt features (Fig. S4). Skeletal olivine is found in LAR 12095, LAR 12240, Tissint, and LAR 06319 (Table 1).

When viewing the central plane orthogonal to the b-axis, mantled dendritic olivine has four primary branches, or dendrites, emanating from the crystal center to its corners {1 0 1} forming a central 'X' shape with approximately 70°/110° angles that are connected by four sides, resulting in an external polyhedral habit (Fig. 2C – 2O and 3). As such, four large melt inclusions are trapped in cavities between the dendrites and the external crystal faces. The dendrites and melt inclusions are ~ 100 μm-thick planar features only viewable along the central a-c plane that are isolated and enclosed by exterior surfaces in 3D (Fig. 3). Mantled dendritic olivine is found both poikilitically enclosed within pyroxene oikocrysts and in the coarse-grained groundmass of the poikilitic shergottites. Mantled dendritic olivine is found in LAR 12011, LAR 06319, NWA 1068, NWA 13227, RBT 04261, NWA 7397, NWA 11043, and NWA 7755 (Table 1).

Chained olivine is similar to the mantled dendritic olivine; there is a primary arm of an "X" along the central [0 1 0] plane but instead of another intersecting arm, there are repeating and parallel branches along the length of the main arm that still intersect at 70°/110° angles (Fig. 2A – 2B and 3). Both the main bar and parallel branches extend towards the crystal corners {1 0 1} and are connected by thicker, mantling olivine forming an external polyhedral habit but much more elongated than the mantled dendritic form. Melt inclusions and, in some areas, infiltrating groundmass, are trapped in cavities between the branching olivine network and the external crystal faces (Fig. 3). When viewing planes orthogonal to the a- and c-axis, it becomes apparent that these features are formed by several olivine linked together. They form "H-shaped" crystals connected by a "cross-bar" that were documented and referred to as chained olivine by (Donaldson, 1976) (Fig. 3). Mantled dendritic and chained olivine morphologies have never been observed in shergottites before. Random 2D slices of olivine with these morphologies would likely not provide a clear indication of their internal structures (Figs. 2, 3, and S5). Only two instances of chained olivine were found in our studied samples; one crystal in NWA 1068 and the other in LAR 12011.

3.2. HYPERLINK "SPS:id::Sec1" Observed trends in olivine crystal population correlated with geochemistry

In addition to discovering new olivine morphologies, we observe systematic textural differences in the olivine crystal populations based on geochemical classification. These olivine trends, described in the following paragraphs, are best observed dynamically by viewing videos of the entire CT dataset, as provided in the supplementary material, rather than as static images.

Olivines with mantled dendritic or chained morphologies are only found in the enriched shergottites and LAR 06319 is the only enriched sample with skeletal olivines ($n = 2$). Skeletal olivines are not found in LAR 12011 (paired with LAR 06319). Within these enriched samples, the largest olivine crystals often have either chained or mantled dendritic (or skeletal in LAR 06319) morphologies and almost every olivine with a long axis of > 1 mm has at least one large and elongated melt inclusion. Such morphologies are common but not universal, as large polyhedral olivine crystals can be found in enriched, poikilitic samples.

The largest olivine crystals in the depleted samples exclusively have equant and polyhedral morphologies with no or only small and spherical melt inclusions. Olivines with skeletal morphology or with large and elongated melt inclusions in the depleted samples are always smaller ($<$1.5 mm long axis).

Nearly every olivine in the intermediate samples is equant polyhedral, and small, spherical melt inclusions are rare. We found no olivine crystals with large and elongated melt inclusions, skeletal, mantled dendritic, or chained morphologies in intermediate samples.

3.3. Olivine crystal length and core composition

To best compare crystal size (Fig. 4), we use a sphere-equivalent radius, (i.e., the radius of a sphere that equals the crystal's volume) instead of a specific axis length because it has been shown that olivine axial ratios can vary as a function of degree of undercooling (Mourey and Shea, 2019). The volume of each crystal was approximated as an ellipsoid with radii equal to the measured crystal axis half-lengths, and thus incorporates melt inclusions and embayments in skeletal and chained olivines. Digitally segmenting and measuring the exact volume of each crystal was not feasible for these samples.

Our data show positive relationships between core Fo_{CT} content and crystal size in the five olivine-phyric shergottites and the poikilitic olivine in poikiltic shergottite RBT 04261 (Fig. 4). LAR 12095 and LAR 12240 show strongly linear relationships and LAR 12011, LAR 06319, and Tissint show linear relationships that flatten at larger crystal sizes. No such relationship exists for the non-poikilitic olivine in RBT 04261 and NWA 7397 and the poikilitic olivine in NWA 7397.

Within enriched and paired olivine-phyric shergottites LAR 12011 and LAR 06319, the mantled dendritic and elongated melt inclusion olivines have similar Fo_{CT} values (combined average $Fo_{CT} = 69$ and 74, respectively) (Fig. 4; Table S2), both of which are elevated compared to the polyhedral olivines (average $Fo_{CT} = 59$ and 63, respectively). The two skeletal olivine, which are only in LAR 06319, have a slightly lower average Fo_{CT} of 70, but have the longest average sphere-equivalent radius length of 0.58 mm. The mantled dendritic olivines have the second largest average sphere-equivalent radius (LAR 12011 = 0.55 mm; LAR 06319 = 0.44 mm) followed by the olivine with an elongated melt inclusion (LAR 12011 = 0.41 mm; LAR 06319 = 0.43 mm) then the polyhedral olivines (LAR 12011 = 0.21 mm; LAR 06319 = 0.19 mm). The chained olivine in NWA 1068 and LAR 12011 were not measured because they were truncated by the sample boundary, but, even in their incomplete form, are still longer than any other crystal in their respective samples.

Of the olivines that are included within the poikilitic assemblages of enriched poikilitic shergottites RBT 04261 and NWA 7397, the mantled dendritic olivines are larger (average sphere-equivalent radius = 0.59 mm and 0.53 mm, respectively) than the olivines with an elongated melt inclusion (0.32 mm and 0.24 mm, respectively) and polyhedral olivines (0.47 mm and 0.26 mm, respectively). Despite the differences in sizes, the mantled dendritic (average $Fo_{CT} = 67$ and 63, respectively), elongated melt inclusion (average $Fo_{CT} = 66$ and 68, respectively), and polyhedral (average $Fo_{CT} = 64$ and 67, respectively) olivines all have

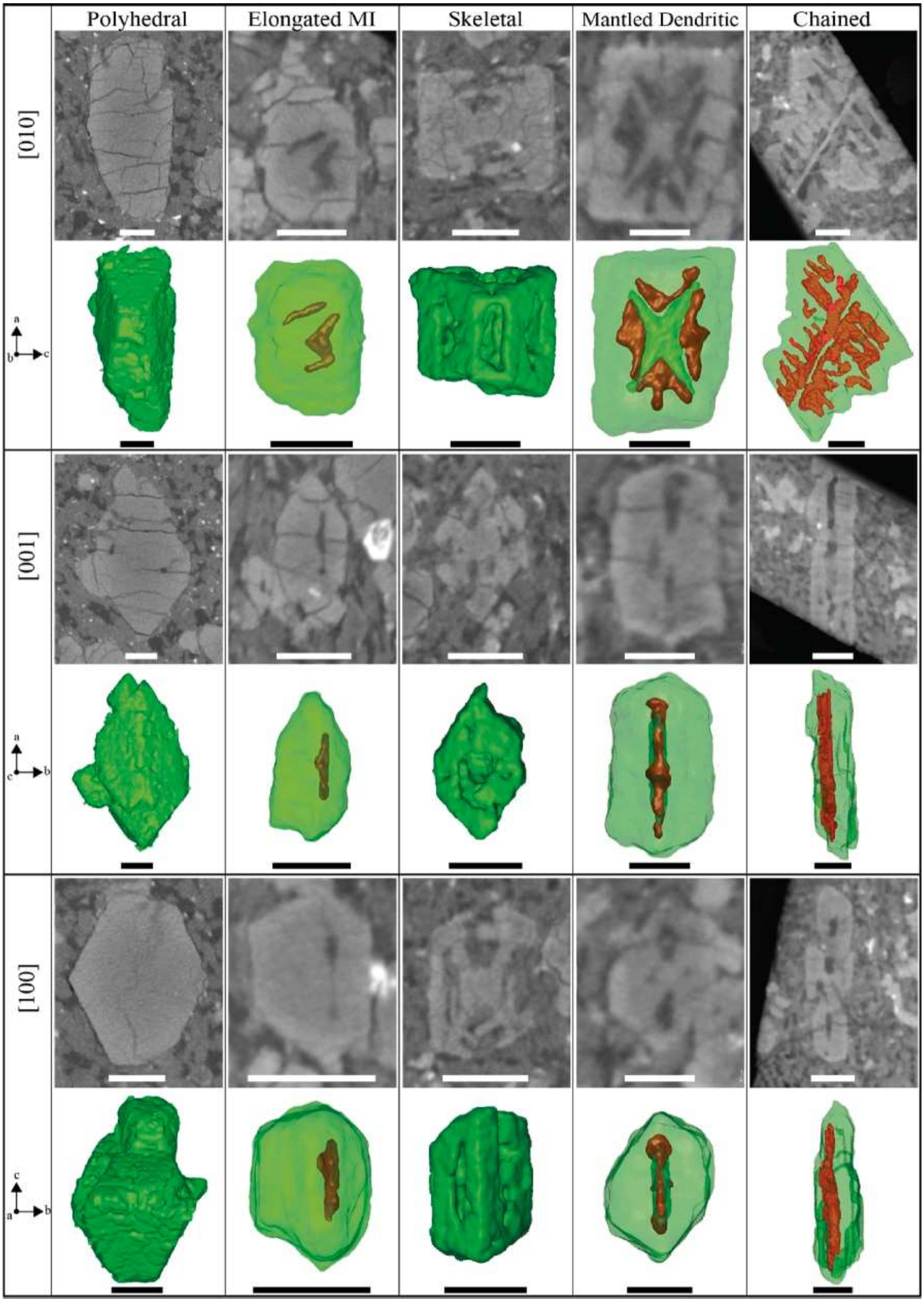

Fig. 3. Orthogonal 2D and 3D views of olivine morphologies. Examples of olivine with polyhedral (LAR 12095), elongated melt inclusion (MI) (LAR 06319), skeletal (Tissint), mantled dendritic (LAR 12011), and chained (NWA 1068) morphologies. Each column is showing the same crystal but from a different orientation. Grayscale CT slices are oriented to expose the central plane along [0 1 0], [0 0 1], and [1 0 0]. 3D volume renderings are oriented in the same viewing direction as the corresponding CT slice above. Dark phases in the CT slices are trapped melt (elongated MI, mantled dendritic, and chained) or infiltrating groundmass (skeletal). Lighter material in the CT slices is olivine. Trapped melt is red in the 3D renderings and olivine is transparent green (elongated MI, mantled dendritic, and chained) or opaque green (polyhedral and skeletal). All scale bars are 0.5 mm.

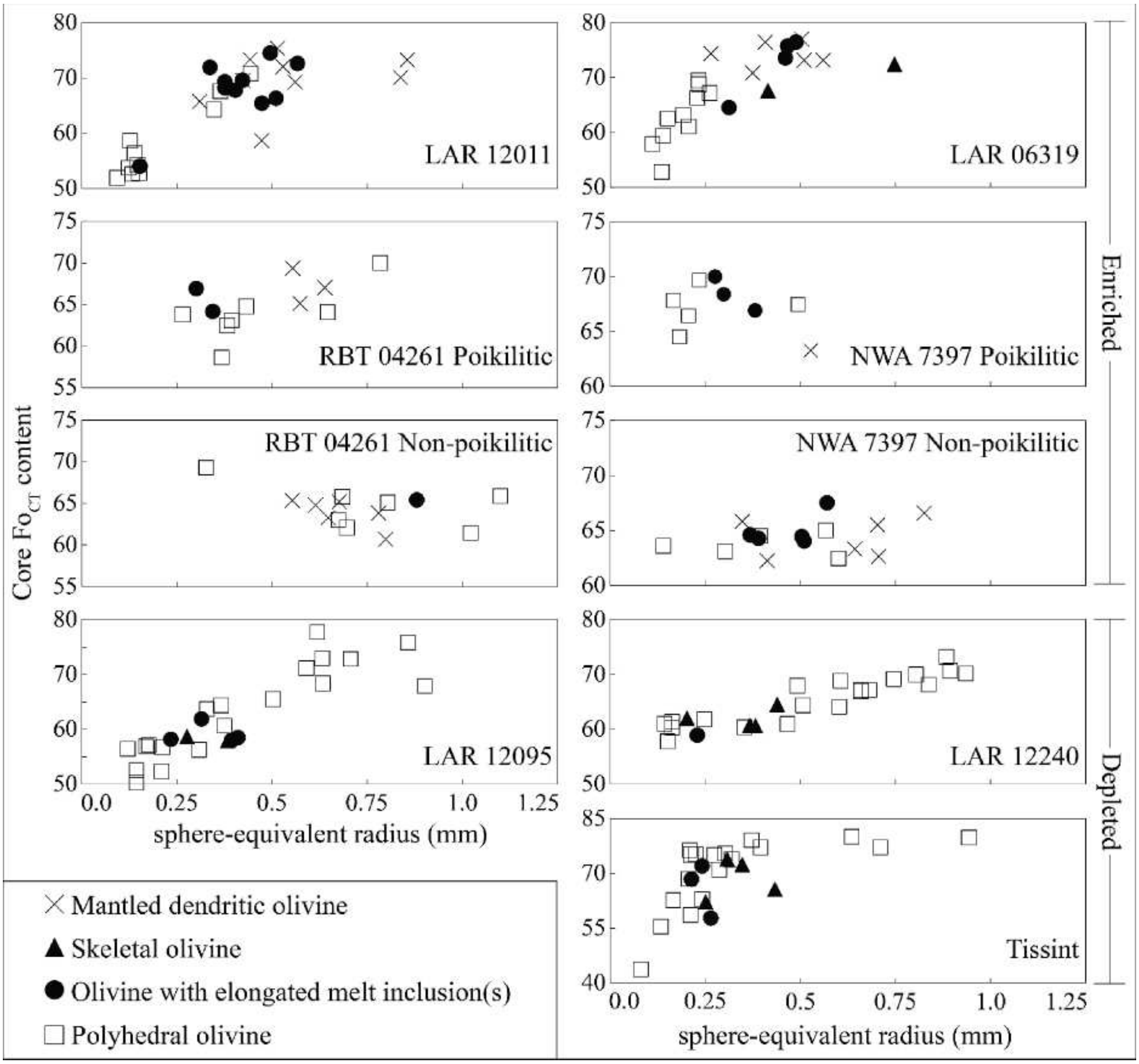

Fig. 4. Approximate Fo$_{CT}$ content at the true crystal core vs. length of sphere-equivalent radius olivines with different morphologies. Sphere-equivalent radius is based on a crystal volume that equals the volume on an ellipsoid with radii lengths corresponding to the measured a-, b-, and c-axis lengths. Polyhedral olivine refers to grains of equant to tabular morphology with few, if any, rounded melt inclusions, and no elongated melt inclusions. Olivine with elongated melt inclusion refers to grains of tabular morphology with elongated melt inclusions and no rapid-growth features (i.e., central dendrites) like those found in the dendritic/skeletal olivine. 'Poikilitic' refers to olivine chadacrysts that are three-dimensionally enclosed by pyroxene oikocrysts and 'non-poikilitic' refers to groundmass olivine. See methods and Table S4 for CT# to Fo$_{CT}$ conversion and Table S2 for Fo$_{CT}$ values and sphere-equivalent radius lengths.

similar average Fo$_{CT}$ values.

The non-poikiltic mantled dendritic, elongated melt inclusion, and polyhedral olivines in both RBT 04261 (average Fo$_{CT}$ content = 64, 64, and 65, respectively; average sphere-equivalent radius length = 0.68 mm, 0.88 mm, and 0.76 mm, respectively) and NWA 7397 (average Fo$_{CT}$ content = 64, 65, and 64, respectively; average sphere-equivalent radius length = 0.61 mm, 0.47 mm, and 0.40 mm) have similar average Fo$_{CT}$ contents and crystal sizes regardless of crystal morphology.

Within the depleted olivine-phyric shergottites LAR 12095, LAR 12240, and Tissint, the polyhedral olivines always represent the highest Fo$_{CT}$ contents and largest sphere-equivalent radius lengths and span the largest ranges of Fo$_{CT}$ contents (LAR 12,095 Fo$_{CT}$ from 50 to 78; LAR 12240 Fo$_{CT}$ from 58 to 73; Tissint Fo$_{CT}$ from 44 to 80) and crystal sizes (LAR 12,095 sphere-equivalent radius lengths from 0.12 mm to 0.90 mm; LAR 12240 sphere-equivalent radius lengths from 0.14 mm to 0.94 mm; Tissint sphere-equivalent radius lengths from 0.08 mm to 0.94 mm). The skeletal and elongated melt inclusion olivines have intermediate sizes and Fo$_{CT}$ contents when compared to the polyhedral olivine, and have a narrower range of Fo$_{CT}$ contents ([combined skeletal and elongated melt inclusion olivine] LAR 12095 Fo$_{CT}$ from 58 to 62; LAR 12240 Fo$_{CT}$ from 59 to 65; Tissint Fo$_{CT}$ from 58 to 74) and sphere-equivalent radius lengths ([combined skeletal and elongated melt inclusion] LAR 12095 sphere-equivalent radius lengths from 0.23 mm to 0.41 mm; LAR 12240 sphere-equivalent radius lengths from 0.20 mm to 0.44 mm; Tissint sphere-equivalent radius lengths from 0.21 mm to 0.43 mm).

When compared to the other olivine morphologies in their respective samples, the rapid-growth olivines (i.e., mantled dendritic or skeletal) in the enriched shergottites generally have the highest Fo$_{CT}$ contents and largest a-axis lengths, but have intermediate Fo$_{CT}$ contents and a-axis lengths in the depleted shergottites. This relationship between crystal size, Fo$_{CT}$ content, and morphology in enriched and depleted samples is consistent with the broader olivine crystal population trends as noted above (sec. 3.2).

There are no systematic relationships between axial ratios and crystal morphology or FoCT content. In all samples, the mantled dendritic, skeletal, and olivine with elongate melt inclusions have some of the lowest a/c axial ratios (Fig. S6) and highest c/b axial ratios (Fig S7), indicating more tabular shapes. However, these morphological types also span most of their respective ranges with many having almost equant a/c and c/b axial ratios. We do not observe systematic preferential growth along the a- or c-axis for the mantled dendritic or skeletal olivine, similar to what was shown in experiments by Mourey and Shea (2019).

4. Discussion

4.1. Rapid growth of olivine

Olivines with a skeletal/hopper, dendritic, or chained morphology reflect rapid growth rates caused by thermodynamic conditions that limit nucleation and supersaturate olivine-forming components in the melt. Experiments have shown that the conditions needed for the growth of these olivine morphologies are overlapping, but dendritic and chained morphologies generally reflect higher degrees of undercooling and faster cooling rates (e.g., Donaldson, 1976; Sunagawa, 1981; Faure et al., 2003). In these early experiments, skeletal morphologies developed when undercooling was between 60 – 90 °C, and dendritic and chained when undercooling was > 70 °C; all three morphologies developed when the cooling rate was > 45 °C/h. Mourey and Shea (2019) and Shea et al. (2019) demonstrated that skeletal olivine can actually form at much more moderate degrees of undercooling, as low as 25 °C. Experiments have not reproduced the mantled dendritic morphology observed here. Mourey and Shea (2019) produced olivine with primary branches connecting to a faceted external shell. However, many of the crystals they show are not fully enclosed, and those that are enclosed have several repeating secondary branches that are parallel to the external shell faces. We propose that the mantled dendritic olivine here, characterized by a single set of primary arms and a fully-enclosed and faceted external shell, developed from an early period of relatively high degree of undercooling followed by partial infilling and maturation during a later period of relaxed undercooling and slower crystal growth.

Moderate to high degrees of undercooling and cooling rates are generally assumed to produce the thermodynamic conditions needed for rapid growth of olivine in terrestrial settings. However, other variables have been experimentally shown to also delay or suppress nucleation, creating conditions needed for rapid growth without a fast cooling rate. Experiments by First et al. (2020) demonstrated that rapid-growth olivine morphologies can form during cooling after the melt was initially heated for different durations at super-liquidus temperatures (≤100 °C above the olivine liquidus) then cooled to 200 °C below liquidus temperature under a moderate cooling rate (25 °C/h). The high degree and duration of superheating more efficiently removes nucleation sites such that, during cooling below the liquidus, homogeneous nucleation is suppressed, and olivine-forming components become supersaturated leading to crystallization of rapid-growth olivine morphologies under a moderate cooling rate (First et al., 2020). Superheating can occur in natural settings through adiabatic decompression from rapid ascent, H_2O flux, or through meteorite impact. Lofgren (1983) also produced olivine with rapid-growth morphologies through a range of low to relatively high cooling rates (0.5 °C/h to 50 °C/h) by varying the number of nucleation sites. These nucleation sites were less than 0.1 μm heterogeneous remnants from superheating and near-complete melting of pre-existing crystals.

The effects of superheating and/or the existence of heterogeneous nucleation sites are challenging, or impossible, to validate in natural settings. Superheating of a crystal-free or pure melt does not produce any chemical or textural evidence, whereas superheating after an earlier period of crystal growth can be inferred from the existence of resorbed inclusions within later-formed crystals. However, partial resorption of earlier phases does not always imply heating above the liquidus temperature as magma mixing can also result in resorption. Additionally, identifying pre-existing sub-micron nucleation sites is problematic. Therefore, we adopt the model that olivines with a skeletal, mantled dendritic, or chained morphology reflect relatively high degrees of undercooling, and that the most likely mechanism driving this undercooling is moderate to fast cooling rates.

4.2. Scenarios that can cause rapid growth

The moderate to high degrees of undercooling and cooling rates needed for rapid growth of megacryst olivine in shergottites are generally unexpected for magmas that are thought to crystallize olivine at or near the martian crust-mantle boundary. In the following sections, we consider potential petrogenetic scenarios that could generate rapid olivine growth at such depths in an arbitrary magma system.

4.2.1. Conductive heat loss

Local thermal gradients are established in magma chambers near the melt-wall rock boundary. Danyushevsky et al. (2004) and Mattioli et al. (2006) present a model wherein these boundaries promoted fast cooling rates, leading to rapid growth of olivine in primitive terrestrial magmas at depth. Thermal gradients are expected to be greatest at the onset of magma chamber growth when initial pulses of melt interact with cooler wall rocks and experience the most rapid conductive heat loss and rapid growth of olivine. Such a model favors a sheet-like magma chamber with a high surface area-to-volume ratio (Brandeis and Jaupart, 1986) and cooler wall-rock temperatures. After construction of the magma chamber, it is expected that a majority of the magma volume would experience a slower cooling rate.

It is worth noting that Mars has an average crustal thickness around 62 km with values that vary from ~ 50 km to 90 km (Plesa et al., 2018) and estimates of crustal geothermal gradients that vary from 5 °C/km to 21 °C/km (Ostwald et al., 2022; and references therein). Parro et al. (2017) calculated a modern average martian heat flow of 20 mW/m^2, suggesting a near-surface geothermal gradient of approximately 10 °C/km that diminishes with depth. Crustal thermal gradients will vary with location and time, but if we assume a linear gradient of 10 °C/km throughout the crust and 0 °C at the surface, the temperature of the wall rocks that surrounded magma chambers where large olivine in shergottites grew (i.e., from 45 km to 90 km deep) would have been approximately 450 °C to 900 °C. A thick and cold crust could explain the possibility of relatively rapid cooling at depth.

4.2.2. Vigorous convection

Vigorous convection in a magma chamber could be created by a large thermal gradient from top to bottom (Martin et al., 1987; Albert et al., 2020), which was posited by Mari et al. (2020) to explain oscillatory P-zoning in megacryst olivine in Tissint. Such an environment would create a transient fast cooling rate followed by a return to near-equilibrium conditions. Thermal gradients are expected to be largest near the upper walls of a magma chamber (Brandeis and Jaupart, 1986).

4.2.3. Volatile Exsolution

Rapid olivine growth can also occur through volatile exsolution. In this scenario, rapid crystallization is not driven by a large degree of undercooling, but by a change in the olivine liquidus temperature caused by volatile exsolution (Hort, 1998; Mattioli et al., 2006; Shea and Hammer, 2013). In terrestrial settings, this process is strongly dependent upon the magma's volatile content and is usually restricted to volatile-rich magmas with intermediate to felsic compositions or other unusually volatile-rich magmas (e.g., kimberlites) (Kuritani, 1999; Gonnermann and Manga, 2013; Büttner et al., 2023).

4.2.4. Magma mixing

Mixing magmas with contrasting temperatures can lead to an overall temperature change of the system and a shift in the olivine liquidus temperature due to a change in the bulk magma composition (Hort, 1998). Rapid growth of olivine can occur in this scenario if the shift in the magma temperature and/or liquidus temperature is large enough. In terrestrial systems, this process typically occurs when a hot, mafic melt interacts with a cooler, intermediate/felsic melt in the upper crust, usually near convergent plate boundaries (Hort, 1998; Mattioli et al., 2006).

4.2.5. Summary

We favor the conductive heat loss model over the vigorous convection, volatile exsolution, and magma mixing models. The survival of the fragile dendritic and skeletal frames observed in our samples suggests that convection may not have been vigorous. Furthermore, if convection is the cause of the P-zoning patterns, it implies multiple cycles of crystal growth, whereas skeletal or mantled dendritic patterns reflect singular episodes of rapid growth. In terrestrial systems, rapid crystallization from volatile exsolution usually occurs in the upper crust, less than around 10 km (Hort, 1998), and in magmas that contain several wt. % dissolved volatile species (usually H_2O and CO_2). The pre-eruptive volatile content of shergottite parent melts is debated, with estimates varying from nominally anhydrous to around 2 wt% (e.g., Udry et al., 2020). Regardless of their abundance, any volatile species would have stayed in solution because the rapid-growth olivine in these samples most likely formed at pressures too high for volatile exsolution.

Mixing of magmas with distinct melt compositions is not supported for some samples based on comparisons between mineral, mineral-hosted melt inclusions, and whole-rock REE contents in Tissint (Balta et al., 2015), LAR 06319/LAR 12011 (Basu Sarbadhikari et al., 2009), and LAR 12095/LAR 12240 (Dunham et al., 2019) that show evidence for closed-system magmatism. However, magma mixing of a cooler, crystal-laden, and more evolved magma with a hotter, crystal-poor, and more primitive magma from the same magmatic system may be possible. Such a scenario describes the origin of antecrystic olivines, which are commonly described in shergottites (e.g., Usui et al., 2008; Balta et al., 2013; Ennis and McSween, 2014; Balta et al., 2015; Dunham et al., 2019). For these shergottites, the evidence of magma mixing is sometimes revealed by P-zoning showing resorbed cores which are later overgrown by newly crystallized olivine that form the overall polyhedral texture.

4.3. Fluctuating thermodynamic conditions

The Fo_{CT} vs. crystal size trends in Fig. 4 are consistent with fractional crystallization processes, where, in the absence of mixing olivine populations, early-formed olivine crystals are expected to have higher-Fo cores and be larger than later-formed crystals. Within the samples in Fig. 4, olivines with skeletal, mantled dendritic, and chained morphologies coexist with tabular and polyhedral olivines of similar or slightly less primitive (i.e., more Fe-rich) compositions that formed in conditions closer to equilibrium. Experimental work has shown that a morphological evolution from polyhedral to tabular to hopper/skeletal to dendritic to chained occurs with increasing degrees of undercooling and cooling rates (i.e., increased disequilibrium) (e.g., Donaldson, 1976; Sunagawa, 1981; Faure et al., 2003). This trend can also be reversed where chained, dendritic, and skeletal olivine can infill and mature into olivine with polyhedral morphologies as the degree of undercooling and cooling rate decreases (Welsch et al., 2013; Welsch et al., 2014; Shea et al., 2015). Consequently, the olivine crystal population in these samples indicates that their parent melts experienced shifting thermodynamic conditions, multiple stages of crystal growth, and a range of crystal growth rates.

During the thermodynamic evolution of their parent melts, some initial fast-growth textures, like high-surface-area dendrites, are protected from breaking, dissolution, and resorption through the formation of the three-dimensionally enclosing polyhedral shells that form the mantled dendritic crystals. Other fast-growth features, like skeletal crystals, start as a skeletal framework that are then variably infilled as a function of the crystal's residence time at near-equilibrium growth conditions (i.e., maturation). An investigation of skeletal olivine growth from Hawaii using the Fe-Mg geospeedometer indicated that skeletal olivine can withstand infilling and maturation even after 4 to 5 months within a high-temperature (1170–1225 °C) melt (Shea et al., 2015). Evidence of early skeletal growth in fully matured/infilled crystals can still potentially be detectable in their chemical zoning patterns (Welsch et al., 2014; Mourey and Shea, 2019). Olivine grains with an external polyhedral morphology but large and elongated or irregular melt inclusions may reflect intermediate disequilibrium conditions, or could result from an initial skeletal or dendritic morphology (i.e., moderate to extreme disequilibrium) and subsequent irregular infilling by slower growth of olivine in conditions closer to equilibrium (Welsch et al., 2013; Welsch et al., 2014). Finally, olivine with tabular to polyhedral morphologies can either reflect growth conditions closest to equilibrium (i.e., low degree of undercooling and slow cooling rate) throughout their entire growth period, or represent fully-matured and infilled skeletal olivine that experienced extended near-equilibrium conditions towards the end of their growth period.

4.4. the relative timing of undercooling in contrasting petrogenetic models

Within the crystallization sequences shown in Fig. 4, we use the occurrence of mantled dendritic and skeletal olivines to mark periods of relatively large degrees of undercooling that occurred during the crystallization history of each sample's parent melt. Combining the morphological and geochemical findings reported here with existing thermodynamic models of magma crystallization, the following discussion provides speculative schematic petrogenetic reconstructions and thermal histories of the shergottite samples considered in this study. The relative thermal histories we note below and the expected growth periods of different olivine morphologies for the enriched and depleted shergottites are illustrated in Fig. 5. We interpret the absence of olivines with rapid-growth morphologies in the intermediate samples as either: (1) an indicator of near-equilibrium growth throughout the olivine crystallization window, or (2) initial growth of skeletal olivines that were then completely infilled and matured during a subsequent extended period of near-equilibrium growth. We favor the first model since large, irregularly-shaped olivine-hosted melt inclusions are rare in these samples, which would be expected in polyhedral olivine that matured from initial skeletal olivine (Wallace et al., 2021). Additionally, there is evidence of at least one early magma recharge event in the form of rounded relict orthopyroxene crystals included within large, Mg-rich olivine in EETA 79001 (Liu et al., 2013), suggesting that any early-formed rapid-growth textures would have likely been partially to completely resorbed.

4.4.1. Early undercooling – geochemically enriched

Based on their FoCT contents and crystal sizes in Fig. 4, the mantled dendritic and skeletal olivines in LAR 12011 and LAR 06319 (and likely the chained olivine in NWA 1068 and LAR 12011 based on their large sizes) formed at the beginning of the olivine crystallization window, requiring the parent melt to have experienced an early period of growth conditions relatively far from equilibrium (i.e., $>$ 70 °C of undercooling and a cooling rate of $>$ 45 °C/h for the growth of chained olivine and $>$ 25 °C undercooling for the growth of skeletal olivine) followed by relaxation back to near-equilibrium conditions. As the earliest magma chamber formed, the initial pulses of melt were introduced to a relatively low-temperature environment and experienced local and near-instantaneous conductive heat loss and rapid growth of olivine at the melt-wall rock boundary. Chained olivine, dendrites within mantled dendritic olivine, and skeletal olivine formed during this time, possibly in this order as the degree of undercooling decreased. This model favors a sheet-like magma chamber with a high surface-area-to-volume ratio (Brandeis and Jaupart, 1986). During growth and development of the magma chamber, additional pulses of melt (i.e., recharge) drove the

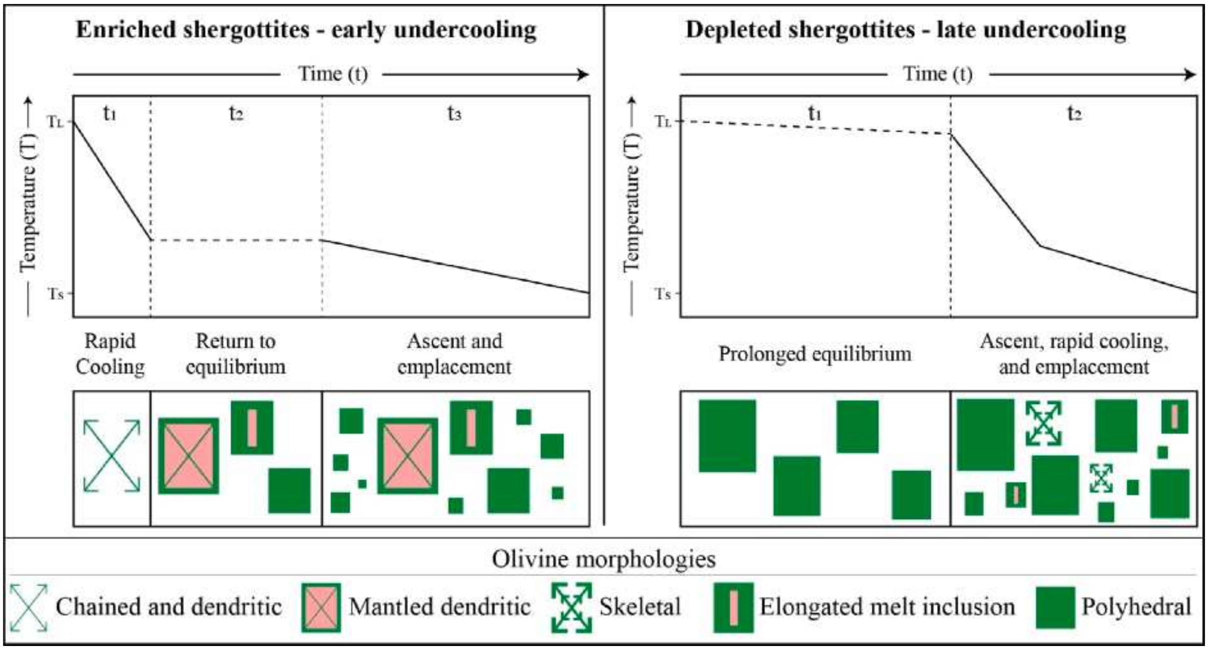

Fig. 5. Shergottite parent magma thermal history and olivine growth schematic for enriched and depleted shergottites. Temperature, time, and slopes of thermal history curves are relative. Dashed portions of the thermal history curves represent potential magma recharge event(s). The timing of rapid cooling during t_2 in depleted shergottites is unknown. T_L = olivine liquidus temperature; T_S = olivine solidus temperature.

magma chamber-wall rock system closer to thermal equilibrium, decreasing the degree of undercooling as well as growth rate. During this period of relaxed undercooling, variable degrees of crystal infilling and maturation occurred, as well as growth of new, polyhedral olivine. Polyhedral shells formed around dendrites to form the mantled dendritic olivine and some skeletal olivine most likely matured into tabular olivine with elongated melt inclusions. The large, skeletal olivines in LAR 06319 are similar to the mantled dendritic olivine, but were unable to form a complete polyhedral shell. These crystals did not completely infill and mature into polyhedral olivine, indicating this later period of relaxed undercooling must have been relatively short-lived, potentially on the order of several months (Shea et al., 2015). Finally, the olivine population and melt ascended and solidified at or near the surface. It is likely that some of the smaller polyhedral olivine initially crystallized during ascent and continued to grow during solidification at or near the surface. This “early undercooling” model establishes a relatively large thermal gradient that requires the surrounding lower crust rocks to be initially at least 70 °C cooler than the olivine liquidus temperature to produce olivines with chained morphologies.

Within the enriched poikilitic samples, the pyroxene oikocrysts enclose olivine chadacrysts with mantled dendritic, tabular, and polyhedral morphologies. The coexistence of these three olivine morphologies, which grew under different thermodynamic conditions, as inclusions within the same pyroxene crystals suggests that olivine mixed and settled into a cumulate pile, after which the poikilitic olivine-pyroxene assemblages formed. Lastly, the presence of rapid-growth olivines with slightly lower Fo-contents within the non-poikilitic region of RBT 04261 and NWA 7397 implies either rapid crystallization during a second, relatively high-undercooling event at shallower depths, possibly in a sill-like magma chamber, or some of the early-formed olivines (dendritic, skeletal, and/or tabular morphologies) were not poikilitically enclosed before ascent, enabling mixing with the later olivine populations that formed at shallower depths. Petrologic and petrographic observations of RBT 04261, NWA 7397, and other poikilitic shergottites corroborate the latter model of mixing early- and late-formed olivines in the non-poikilitic region (Usui et al., 2010; Rahib et al., 2019).

This early undercooling model is thermodynamically complicated since the fragile, rapid-growth textures with high surface areas would likely be partially to completely resorbed due to decompression shifting the melt closer to its liquidus during ascent through the crust. The olivine crystals with chained, mantled dendritic, and elongated melt inclusion morphologies in the olivine-phyric shergottites are protected by their exterior polyhedral shells and the pyroxene oikocrysts in the enriched poikilitic shergottites encapsulated and protected the olivine chadacrysts. However, the preservation of large, Mg-rich skeletal olivine in LAR 06319 is challenging to reconcile with this current model as they are expected to break or dissolve during the subsequent evolution of their parent melt. Possible mechanisms to explain their survival could be: (1) that the reentrant features of the skeletal framework trapped melt and/or crystals to create a localized region of thermal and chemical equilibrium; (2) ascent rates and heat loss were balanced such that the crystal and melt stayed in thermal equilibrium; or (3) these crystals actually formed at shallower depths. The results from this study cannot answer this question but do reveal that the enriched shergottites’ thermal histories are complex.

4.4.2. Late undercooling – geochemically depleted

Within depleted samples, the large, high Fo_{CT} polyhedral olivines initially grew in near-equilibrium conditions, after which a change to the thermal environment resulted in moderate to high undercooling of 25 °C – 60 °C, prompting the growth of skeletal olivines. To produce this thermal history, a possible scenario is that the parent melt initially ponded in a magma chamber within the lower crust and experienced an extended period of near-equilibrium conditions. During this period, the parent melt experienced at least once cycle of growth, dissolution, then regrowth, most likely from magma recharge, based on the presence of resorbed olivine and orthopyroxene inclusions within high-Fo megacryst olivine (Balta et al., 2015; Dunham et al., 2019). Any morphological evidence for an initial high undercooling event would have been partially to completely infilled and/or resorbed during this extended near-equilibrium period. Next, the melt and high-Fo polyhedral crystals ascended to shallower depths in the crust and experienced a relatively large degree of undercooling and a moderate to high cooling rate in the magma conduit or a secondary magma chamber leading to the growth of skeletal olivine (Mourey and Shea, 2019; Salas et al., 2021). We cannot discern the exact timing of undercooling, but size and core FoCT content relationships indicate that olivine with polyhedral and tabular morphologies continued to form after the skeletal olivines (Fig. 4) or from variable infilling and maturation of skeletal olivines, suggesting a return to conditions closer to equilibrium or concurrent equilibrium and disequilibrium growth within the same magma. To prevent complete infilling and maturation of skeletal olivine, this second period of olivine growth must have been relatively short-lived (Shea et al., 2015). This "late undercooling" scenario aligns with previous models, which propose that olivines with high Fo-content in Tissint grew over extended periods in a quiescent magma chamber, where Fe-Mg zoning was homogenized through diffusion, and later, more rapid cooling produced thin olivine rims with low Fo content (Balta et al., 2015; Liu et al., 2016).

4.5. Thermal histories linked to planet-wide processes

The petrogenetic models above are simplified and do not expand on the many nuances of magma crystallization and are constrained by previous thermobarometric investigations and calculated crystallization sequences indicating that Mg-rich olivine is the first silicate phase to form while in staging magma chambers in the lower crust (Musselwhite et al., 2006; Usui et al., 2008; Filiberto et al., 2010; Usui et al., 2012; Balta et al., 2013; Gross et al., 2013; Howarth et al., 2014; Balta et al., 2015; Basu Sarbadhikari et al., 2016; Liu et al., 2016; Dunham et al., 2019; Rahib et al., 2019; Udry et al., 2020). Olivine continues to nucleate and grow throughout a large portion of their respective parent melts' petrogenetic histories. The exact thermal histories and olivine growth sequences are certainly more complicated that we present here, but the focus of this work is to document and characterize new crystal textures and the relative timing of crystallization sequences. Our findings indicate that the geochemically depleted, intermediate, and enriched shergottite parent melts experienced different thermal histories. Possible mechanisms to explain an early, relatively large degree of undercooling for enriched samples include: (1) prior to crystallization, the enriched parent magmas were initially closer to the olivine liquidus temperature (i.e., cooler) than the depleted and intermediate magmas at a given depth before ponding and rapid cooling in a magma chamber; (2) the enriched magmas initially ponded at shallower depths where the surrounding crust was cooler; or (3) enriched magmas ponded in magma chambers with a higher surface-area-to-volume ratio. A combination of these mechanisms may be possible and implies that enriched shergottites are from volcanic areas with a lower geothermal gradient and/or that depth of initial crystallization is shallower than the depleted shergottites.

An elevated local geothermal gradient for the depleted shergottites is consistent with the study by Lapen et al. (2017), who showed that a group of at least eleven depleted shergottites with the same ejection age (1.1 Ma) have crystallization ages that span over 2 billion years (2.4 Ga to 0.145 Ga), suggesting they are likely from the same long-lived and episodic volcanic system. Local wall-rock temperatures are expected to be higher at greater depths and/or near volcanic centers (Ostwald et al., 2022). No such temporal, geochemical, or spatial relationship has been found for the enriched or intermediate shergottites, which are generally younger (225 to 165 Ma and 346 to 150 Ma, respectively; Udry et al. (2020) and references therein), possibly reflecting transient volcanic systems.

4.6. Ubiquity of rapid-growth olivine morphologies in martian igneous rocks

The proposed early- and late-undercooling petrogenetic models are based on the crystallization sequences measured in seven samples in Fig. 4. These crystallization histories are likely consistent and applicable to the other samples in this study of similar geochemical classification whose crystal size and core Fo_{CT} content were not measured. The broader trends in olivine crystal populations based on geochemical classification noted in all samples in section 3.2 match the results in Fig. 4. Our method is also internally consistent based on similar results from paired samples LAR 06319/LAR 12,011 and LAR 12095/LAR 12240.

While the fourteen samples in this study represent a small fraction of the total number of shergottites that contain large, early-formed olivine identified to date, olivines with rapid-growth morphologies are likely present in more specimens. That such morphologies have not been widely recognized may be attributed to limitations of studying randomly sliced 2D petrographic sections. Unless a 2D slice is fortuitously oriented, it will miss the characteristic arrangement of the melt inclusions (e.g., Figs. 2 and 3) and sparse skeletal grains. The true spatial context of inclusions and mineral morphologies in such grains is only reliably revealed through 3D observation. We provide guidance on how to recognize rapid-growth morphologies in 2D sections based on the projection from 3D data in the supplementary text. By applying this approach, we identified additional shergottites that likely include skeletal and mantled dendritic olivines (Figs. S8-S16, Table S5).

Finally, rapid-growth olivines may not be limited to just shergottites, which mostly represent relatively young volcanic activity (~2.4 Ga to 150 Ma) (e.g., Udry et al., 2020). Olivine grains with multiple, elongated melt inclusions are often present in 1.3 Ga chassignites, which are dunites (Hewins et al., 2020) (Fig. S17). Hopper/skeletal olivines with large melt inclusions have recently been identified in the olivine cumulate rocks from the ~ 3.9 Ga Séítah formation within Jezero crater (Liu et al., 2022). Collectively, these results suggest that the rapid growth of olivine due to relatively high degrees of undercooling at depth may be a ubiquitous feature of mafic magmatism throughout the evolution of Mars.

5. Conclusions

We report the ubiquitous presence of olivines with crystal morphologies reflecting rapid growth from moderate to high degrees of undercooling in an X-ray CT investigation of fourteen shergottites that contain large, early-formed olivine crystals. We present a novel approach to estimate sample-wide crystal core forsterite compositions and crystal sizes to constrain the timing of rapid olivine growth relative to other olivine crystals. Geochemically enriched shergottites experience rapid growth at the beginning of olivine crystallization, whereas the depleted shergottites experience an initial period of equilibrium growth followed by a period of rapid growth. When combined with previous thermobarometric work, these results indicate that unexpectedly high undercooling of magma occurs deep in the martian crust, providing new insights into martian magmatism and thermal structure. Furthermore, our results suggest that there are systematic differences in the crystallization histories of the geochemically enriched, intermediate, and depleted shergottites.

CRediT authorship contribution statement

S.A. Eckley: Conceptualization, Data curation, Formal analysis, Investigation, Methodology, Visualization, Writing – original draft, Writing – review & editing. **R.A. Ketcham:** Conceptualization, Methodology, Supervision, Validation, Visualization, Writing – original draft, Writing – review & editing. **Y. Liu:** Writing – original draft, Writing – review & editing, Conceptualization, Formal analysis, Investigation, Methodology, Resources, Visualization. **A. Udry:** Resources, Writing – original draft, Writing – review & editing. **J. Gross:** Writing – original draft, Writing – review & editing, Resources.

Declaration of competing interest

The authors declare that they have no known competing financial interests or personal relationships that could have appeared to influence the work reported in this paper.

Data availability

Data needed to reach the conclusions on this work can be found via a Mendeley data repository: https://doi.org/10.17632/b2w3t59sgg.1. Supplementary movies S1 – S22 show olivine in 3D as well a video of each sample's CT slices. CT data will be made available upon request from the corresponding author.

Acknowledgements

We thank the Astromaterials X-ray CT Lab at NASA – Johnson Space Center (JSC) and the University of Texas High-Resolution X-ray CT Lab (UTCT) for the collection of X-ray CT data and Linda Welzenbach-Fries and Marc Fries for loaning a sample of 'Tissint'. XCT data for RBT 04261 were produced for Astromaterials 3D in NASA's Acquisition & Curation Office and were funded by NASA Planetary Data Archiving, Restoration, and Tools Program, Proposal No.: 15-PDART15_2-0041. US Antarctic meteorite samples are recovered by the Antarctic Search for Meteorites (ANSMET) program which has been funded by NSF and NASA and characterized and curated by the Department of Mineral Sciences of the Smithsonian Institution and Astromaterials Acquisition and Curation Office (AACO) at NASA Johnson Space Center. UTCT is partially supported through NSF-IF grant EAR-1762458 to RAK. YL is partially supported by the NASA SSW grant (80NM0018F0612). YL's research on this manuscript was performed at the Jet Propulsion Laboratory, California Institute of Technology, under a contract with NASA Administration (80NM0018D0004).

Appendix A. Supplementary material

The supplementary materials include a description of how samples were acquired, details for crystallographic indexing, electron probe microanalysis of LAR 12095 and LAR 12011 for Fo_{CT} conversion, and guidance for identifying rapid-growth olivine in 2D thin sections. Figs. S1 – S3 show Fo_{CT} conversion comparisons. Figs. S4 and S5 show examples of randomly oriented CT slices through skeletal and mantled dendritic olivines, respectively. Figs. S6 and S7 show Fo_{CT} vs. a/c and c/b axial ratios, respectively. Figs. S8 – S17 show 2D thin section images modified from the literature that have the characteristic arrangement of melt inclusions or external morphologies that most likely indicate they are olivine with rapid-growth morphologies. Table S1 contains CT scanning information; table S2 contains olivine sizes, core CT #, and converted core Fo content; table S3 contains EPMA data for LAR 12095 and LAR 12011; table S4 contains information on converting CT # to Fo content; and table S4 contains a list of Martian igneous rocks that likely have olivine with rapid growth morphologies. Supplementary material to this article can be found online at https://doi.org/10.1016/j.gca.2024.04.006.

References

Albert, H., Larrea, P., Costa, F., Widom, E., Siebe, C., 2020. Crystals reveal magma convection and melt transport in dyke-fed eruptions. Sci. Rep. 10, 11632.

Balta, J.B., Sanborn, M., McSween, H.Y., Wadhwa, M., 2013. Magmatic history and parental melt composition of olivine-phyric shergottite LAR 06319: importance of magmatic degassing and olivine antecrysts in Martian magmatism. Meteorit. Planet. Sci. 48, 1359–1382.

Balta, J.B., Sanborn, M.E., Udry, A., Wadhwa, M., McSween, H.Y., 2015. Petrology and trace element geochemistry of tissint, the newest shergottite fall. Meteorit. Planet. Sci. 50, 63–85.

Barrat, J., Jambon, A., Bohn, M., Gillet, P., Sautter, V., Göpel, C., Lesourd, M., Keller, F., 2002. Petrology and chemistry of the picritic shergottite north West Africa 1068 (NWA 1068). Geochim. Cosmochim. Acta 66, 3505–3518.

Basu Sarbadhikari, A.B., Day, J.M., Liu, Y., Rumble III, D., Taylor, L.A., 2009. Petrogenesis of olivine-phyric shergottite Larkman nunatak 06319: implications for enriched components in Martian basalts. Geochim. Cosmochim. Acta 73, 2190–2214.

Basu Sarbadhikari, A.B., Babu, E., Vijaya Kumar, T., Chennaoui Aoudjehane, H., 2016. Martian meteorite tissint records unique petrogenesis among the depleted shergottites. Meteorit. Planet. Sci. 51, 1588–1610.

Benaroya, S., Gross, J., Burger, P., Righter, M., Lapen, T.J., Eckley, S.A., 2024. Petrogenesis of a new type of intrusive shergottite: olivine-gabbroic Northwest Africa 13227. Geochim. Cosmochim. Acta 370, 41–65.

Brandeis, G., Jaupart, C., 1986. On the interaction between convection and crystallization in cooling magma chambers. Earth Planet. Sci. Lett. 77, 345–361.

Büttner, S., van Huyssteen, A., Marima, E., du Plessis, A., Tshibalanganda, M., Schmidt, C., Howarth, G., 2023. The capturing and decompression of melt inclusions in olivine and ilmenite megacrysts from the Monastery kimberlite, South Africa. Gond. Res. 115, 81–97.

Danyushevsky, L.V., Leslie, R.A., Crawford, A.J., Durance, P., 2004. Melt inclusions in primitive olivine phenocrysts: the role of localized reaction processes in the origin of anomalous compositions. J. Petrol. 45, 2531–2553.

Donaldson, C.H., 1976. An experimental investigation of olivine morphology. Cont. Mineral. Petrol. 57, 187–213.

Dunham, E.T., Balta, J.B., Wadhwa, M., Sharp, T.G., McSween Jr, H.Y., 2019. Petrology and geochemistry of olivine-phyric shergottites LAR 12095 and LAR 12240: implications for their petrogenetic history on Mars. Meteorit. Planet. Sci. 54, 811–835.

Ennis, M.E., McSween, H.Y., 2014. Crystallization kinetics of olivine-phyric shergottites. Meteorit. Planet. Sci. 49, 1440–1455.

Faure, F., Trolliard, G., Nicollet, C., Montel, J.-M., 2003. A developmental model of olivine morphology as a function of the cooling rate and the degree of undercooling. Cont. Mineral. Petrol. 145, 251–263.

Filiberto, J., Musselwhite, D.S., Gross, J., Burgess, K., Le, L., Treiman, A.H., 2010. Experimental petrology, crystallization history, and parental magma characteristics of olivine-phyric shergottite NWA 1068: implications for the petrogenesis of "enriched" olivine-phyric shergottites. Meteorit. Planet. Sci. 45, 1258–1270.

First, E.C., Leonhardi, T.C., Hammer, J.E., 2020. Effects of superheating magnitude on olivine growth. Cont. Mineral. Petrol. 175, 1–14.

Gonnermann, H.M., Manga, M., 2013. Dynamics of magma ascent. Modeling volcanic processes. Phys. Math. Volcan 55.

Goodrich, C.A., 2002. Olivine-phyric Martian basalts: a new type of shergottite. Meteorit. Planet. Sci. 37, B31–B34.

Goodrich, C.A., 2003. Petrogenesis of olivine-phyric shergottites sayh al uhaymir 005 and elephant Moraine A79001 lithology a. Geochim. Cosmochim. Acta 67, 3735–3772.

Gross, J., Treiman, A.H., Filiberto, J., Herd, C.D., 2011. Primitive olivine-phyric shergottite NWA 5789: petrography, mineral chemistry, and cooling history imply a magma similar to Yamato-980459. Meteorit. Planet. Sci. 46, 116–133.

Gross, J., Filiberto, J., Herd, C.D., Daswani, M.M., Schwenzer, S.P., Treiman, A.H., 2013. Petrography, mineral chemistry, and crystallization history of olivine-phyric shergottite NWA 6234: a new melt composition. Meteorit. Planet. Sci. 48, 854–871.

Hewins, R., Humayun, M., Barrat, J.-A., Zanda, B., Lorand, J.-P., Pont, S., Assayag, N., Cartigny, P., Yang, S., Sautter, V., 2020. Northwest Africa 8694, a ferroan chassignite: bridging the gap between nakhlites and chassignites. Geochim. Cosmochim. Acta 282, 201–226.

Hort, M., 1998. Abrupt change in magma liquidus temperature because of volatile loss or magma mixing: effects on nucleation, crystal growth and thermal history of the magma. J. Petrol. 39, 1063–1076.

Howarth, G.H., Pernet-Fisher, J.F., Balta, J.B., Barry, P.H., Bodnar, R.J., Taylor, L.A., 2014. Two-stage polybaric formation of the new enriched, pyroxene-oikocrystic, lherzolitic shergottite, NWA 7397. Meteorit. Planet. Sci. 49, 1812–1830.

Ketcham, R.A., Carlson, W.D., 2001. Acquisition, optimization and interpretation of X-ray computed tomographic imagery: applications to the geosciences. Comput. Geosci. 27, 381–400.

Ketcham, R., Mote, A., 2019. Accurate measurement of small features in X-ray CT data volumes, demonstrated using gold grains. J. Geophys. res.: solid. Earth.

Kuritani, T., 1999. Phenocryst crystallization during ascent of alkali basalt magma at rishiri volcano, northern Japan. J. Volcan. Geothem. Res. 88, 77–97.

Lapen, T.J., Righter, M., Andreasen, R., Irving, A.J., Satkoski, A.M., Beard, B.L., Nishiizumi, K., Jull, A.T., Caffee, M.W., 2017. Two billion years of magmatism recorded from a single Mars meteorite ejection site. Sci. Adv. 3, e1600922.

Liu, Y., Balta, J.B., Goodrich, C.A., McSween Jr, H.Y., Taylor, L.A., 2013. New constraints on the formation of shergottite elephant Moraine 79001 lithology a. Geochim. Cosmochim. Acta 108, 1–20.

Liu, Y., Baziotis, I.P., Asimow, P.D., Bodnar, R.J., Taylor, L.A., 2016. Mineral chemistry of the tissint meteorite: indications of two-stage crystallization in a closed system. Meteorit. Planet. Sci. 51, 2293–2315.

Liu, Y., Tice, M., Schmidt, M., Treiman, A., Kizovski, T., Hurowitz, J., Allwood, A., Henneke, J., Pedersen, D., VanBommel, S., 2022. An olivine cumulate outcrop on the floor of jezero crater. Mars, Sci, p. 2756.

Lofgren, G.E., 1983. Effect of heterogeneous nucleation on basaltic textures: a dynamic crystallization study. J. Petrol. 24, 229–255.

Mari, N., Hallis, L.J., Daly, L., Lee, M.R., 2020. Convective activity in a Martian magma chamber recorded by P-zoning in tissint olivine. Meteorit. Planet. Sci. 55, 1057–1072.

Martin, D., Griffiths, R.W., Campbell, I.H., 1987. Compositional and thermal convection in magma chambers. Cont. Mineral. Petrol. 96, 465–475.

Mattioli, M., Renzulli, A., Menna, M., Holm, P.M., 2006. Rapid ascent and contamination of magmas through the thick crust of the CVZ (Andes, ollagüe region): evidence from a nearly aphyric high-K andesite with skeletal olivines. J. Volcan. Geotherm. Res. 158, 87–105.

Milman-Barris, M.S., Beckett, J.R., Baker, M.B., Hofmann, A.E., Morgan, Z., Crowley, M. R., Vielzeuf, D., Stolper, E., 2008. Zoning of phosphorus in igneous olivine. Cont. Mineral. Petrol. 155, 739–765.

Mourey, A.J., Shea, T., 2019. Forming olivine phenocrysts in basalt: a 3D characterization of growth rates in laboratory experiments. Front. Earth Sci. 7, 300.

Musselwhite, D.S., Dalton, H.A., Kiefer, W.S., Treiman, A.H., 2006. Experimental petrology of the basaltic shergottite Yamato-980459: implications for the thermal structure of the Martian mantle. Meteorit. Planet. Sci. 41, 1271–1290.

Ostwald, A., Udry, A., Valerie, P., Gazel, E., Wu, P., 2022. The role of assimilation and fractional crystallization in the evolution of the Mars crust. Earth Planet. Sci. Lett. 585, 117554.

Parro, L.M., Jiménez-Díaz, A., Mansilla, F., Ruiz, J., 2017. Present-day heat flow model on Mars. Sci. Reports 7 (1), 45629.

Peslier, A., Hnatyshin, D., Herd, C., Walton, E., Brandon, A., Lapen, T., Shafer, J., 2010. Crystallization, melt inclusion, and redox history of a Martian meteorite: olivine-phyric shergottite Larkman nunatak 06319. Geochim. Cosmochim. Acta 74, 4543–4576.

Plesa, A.C., Padovan, S., Tosi, N., Breuer, D., Grott, M., Wieczorek, M.A., Spohn, T., Smrekar, S.E., Banerdt, W.B., 2018. The thermal state and interior structure of Mars. Geophys. Res. Lett. 22, 12–198.

Rahib, R.R., Udry, A., Howarth, G.H., Gross, J., Paquet, M., Combs, L.M., Laczniak, D.L., Day, J.M., 2019. Mantle source to near-surface emplacement of enriched and intermediate poikilitic shergottites in Mars. Geochim. Cosmochim. Acta 266, 463–496.

Salas, P., Ruprecht, P., Hernández, L., Rabbia, O., 2021. Out-of-sequence skeletal growth causing oscillatory zoning in arc olivines. Nat. Comm. 12, 1–14.

Shafer, J., Brandon, A., Lapen, T., Righter, M., Peslier, A., Beard, B., 2010. Trace element systematics and 147Sm–143Nd and 176Lu–176Hf ages of Larkman nunatak 06319: closed-system fractional crystallization of an enriched shergottite magma. Geochim. Cosmochim. Acta 74, 7307–7328.

Shea, T., Hammer, J.E., 2013. Kinetics of cooling-and decompression-induced crystallization in hydrous mafic-intermediate magmas. J. Volcan. Geotherm. Res. 260, 127–145.

Shea, T., Lynn, K.J., Garcia, M.O., 2015. Cracking the olivine zoning code: distinguishing between crystal growth and diffusion. Geol. 43, 935–938.

Shea, T., Hammer, J.E., Hellebrand, E., Mourey, A.J., Costa, F., First, E.C., Lynn, K.J., Melnik, O., 2019. Phosphorus and aluminum zoning in olivine: contrasting behavior of two nominally incompatible trace elements. Cont. Mineral. Petrol. 174, 1–24.

Sunagawa, I., 1981. Characteristics of crystal growth in nature as seen from the morphology of mineral crystals. Bull. De Minéral. 104, 81–87.

Symes, S.J., Borg, L.E., Shearer, C.K., Irving, A.J., 2008. The age of the Martian meteorite Northwest Africa 1195 and the differentiation history of the shergottites. Geochim. Cosmochim. Acta 72, 1696–1710.

Udry, A., Howarth, G.H., Herd, C., Day, J.M., Lapen, T.J., Filiberto, J., 2020. What martian meteorites reveal about the interior and surface of Mars. J. Geophys. Res.: Planets 125 e2020JE006523.

Usui, T., McSween Jr, H.Y., Floss, C., 2008. Petrogenesis of olivine-phyric shergottite Yamato 980459, revisited. Geochim. Cosmochim. Acta 72, 1711–1730.

Usui, T., Sanborn, M., Wadhwa, M., McSween Jr, H.Y., 2010. Petrology and trace element geochemistry of Robert massif 04261 and 04262 meteorites, the first examples of geochemically enriched lherzolitic shergottites. Geochim. Cosmochim. Acta 74, 7283–7306.

Usui, T., Alexander, C.M.D., Wang, J., Simon, J.I., Jones, J.H., 2012. Origin of water and mantle–crust interactions on Mars inferred from hydrogen isotopes and volatile element abundances of olivine-hosted melt inclusions of primitive shergottites. Earth Planet. Sci. Lett. 357, 119–129.

Wallace, P.J., Plank, T., Bodnar, R.J., Gaetani, G.A., Shea, T., 2021. Olivine-hosted melt inclusions: a microscopic perspective on a complex magmatic world. An. Rev. of Earth and Planet. Sci. 49, 465–494.

Welsch, B., Faure, F., Famin, V., Baronnet, A., Bachèlery, P., 2013. Dendritic crystallization: a single process for all the textures of olivine in basalts? J. Petrol. 54, 539–574.

Welsch, B., Hammer, J., Hellebrand, E., 2014. Phosphorus zoning reveals dendritic architecture of olivine. Geol. 42, 867–870.

Xing, C.-M., Wang, C.Y., Tan, W., 2017. Disequilibrium growth of olivine in mafic magmas revealed by phosphorus zoning patterns of olivine from mafic–ultramafic intrusions. Earth Planet. Sci. Lett. 479, 108–119.